RMP Effects On Pedestal Plasma Transport

J.D. Callen,[a] A.J. Cole,[b] C.C. Hegna,[a] S. Mordijck,[c] R.A. Moyer[d]

[a]University of Wisconsin, [b]Columbia University, [c]William and Mary, [d]University of California-San Diego

Edge-III session, U.S. Transport Task Force Workshop, Annapolis, MD, April 10–13, 2012

Issue To Be Addressed:

Is RMP-flutter-induced[1] pedestal plasma transport important?[2]

Theses:

- **At pedestal top[2] RMPs reduce $|\vec{\nabla} T_e|$ more than $|\vec{\nabla} n_e|$, with changes $\propto I_{\rm coil}^2$; they also change plasma toroidal rotation $\Omega_{\rm t}$.**
- **Flow-screening averts stochasticity-induced[3] but not flutter[1] xport.**
- **RMP-flutter-induced transport[1] might cause observed transport.[2]**
- **Model implications are different at low[4] & high[5] collisionality.**

[1]J.D. Callen, "Drift-Wave Turbulence Effects on Magnetic Structure and Plasma Transport in Tokamaks," Phys. Rev. Lett. **39**, 1540 (1977).
[2]J.D. Callen, A.J. Cole, C.C. Hegna, S. Mordijck, R.A. Moyer, "RMP effects on pedestal structure and ELMs," UW-CPTC 11-13R (to be pub. in NF).
[3]A.B. Rechester and M.N. Rosenbluth, "Electron heat transport in a tokamak with destroyed magnetic surfaces," Phys. Rev. Lett. **40**, 38 (1978).
[4]T.E. Evans et al., "RMP ELM suppression in DIII-D plasmas with ITER similar shapes and collisionalities," Nucl. Fusion **48**, 024002 (2008).
[5]W. Suttrop et al., "Studies of edge localized mode mitigation with new active in-vessel saddle coils in ASDEX Upgrade," PPCF **53**, 124014 (2011).

RMPs Reduce Pressure Gradient At Pedestal Top

- RMP-induced reductions in $|\vec{\nabla} P|$ are:

  small in core,

  largest at the pedestal top, and

  small (increase!?) at the edge.

- Key transport issue for ELM suppression is:

  How do RMPs reduce $|\vec{\nabla} P|$ at the pedestal top?

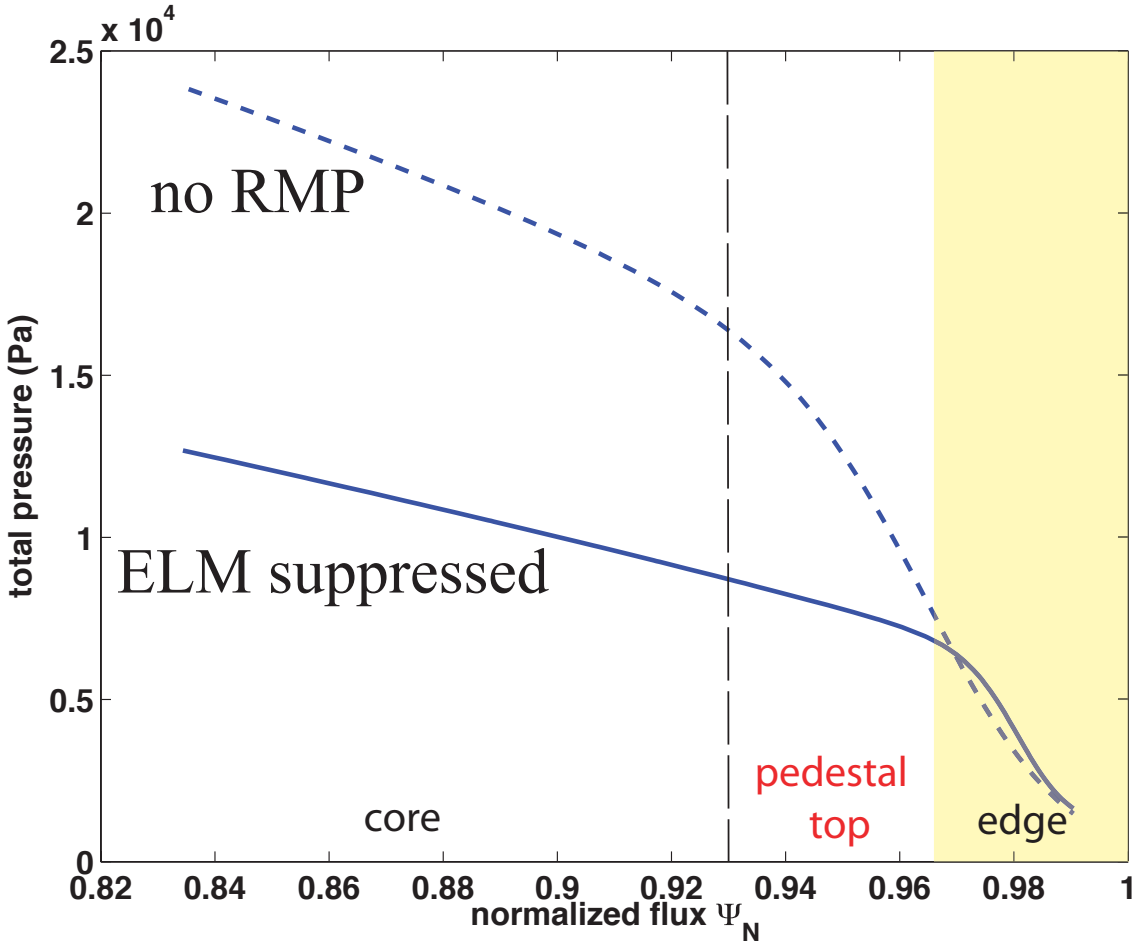

Figure 1: **Edge pressure profile without/with RMP ELM suppression. Courtesy of O. Schmitz, R. Nazikian, 2011.**

RMPs Increase T_e, n_e Gradient Lengths At Pedestal Top

- T_e, n_e gradient length ratios with RMPs to wo (sym) $\propto \chi_e$, D:

$$\frac{[L_{Te}]_{\rm RMP}}{[L_{Te}]_{\rm sym}} \simeq \frac{\chi_e^{\rm RMP} + \chi_e^{\rm sym}}{\chi_e^{\rm sym}};$$

plus a similar formula for L_n, $D^{\rm RMP}$.

- Apparently RMPs increase:

  χ_e by $\lesssim \times 6$,

  D by $\lesssim \times 2$.

- Changes peak at pedestal top:

  $0.93 \lesssim \Psi_N \lesssim 0.97$,

  near 11/3 surface.

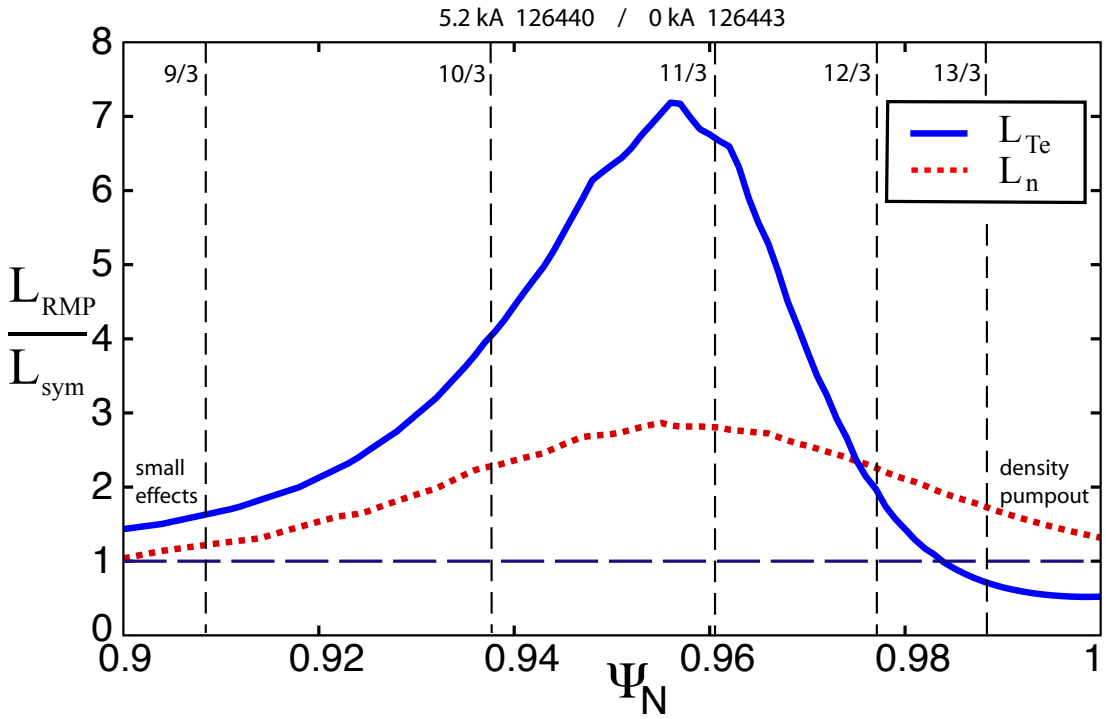

Figure 2: **Ratio of T_e and n_e gradient scale lengths with RMPs to without (sym) versus radius.[2]**

Peak Of RMP-induced Extra Transport $\propto I^2_{\rm coil}$

- Peak T_e, n_e gradient length ratios scale approximately with $I^2_{\rm coil}$.
- Peak L_{Te} ratio increases $\sim 3\times$ more than peak L_n ratio does, which indicates $D^{\rm RMP}/\chi_e^{\rm RMP} \sim 1/3$.

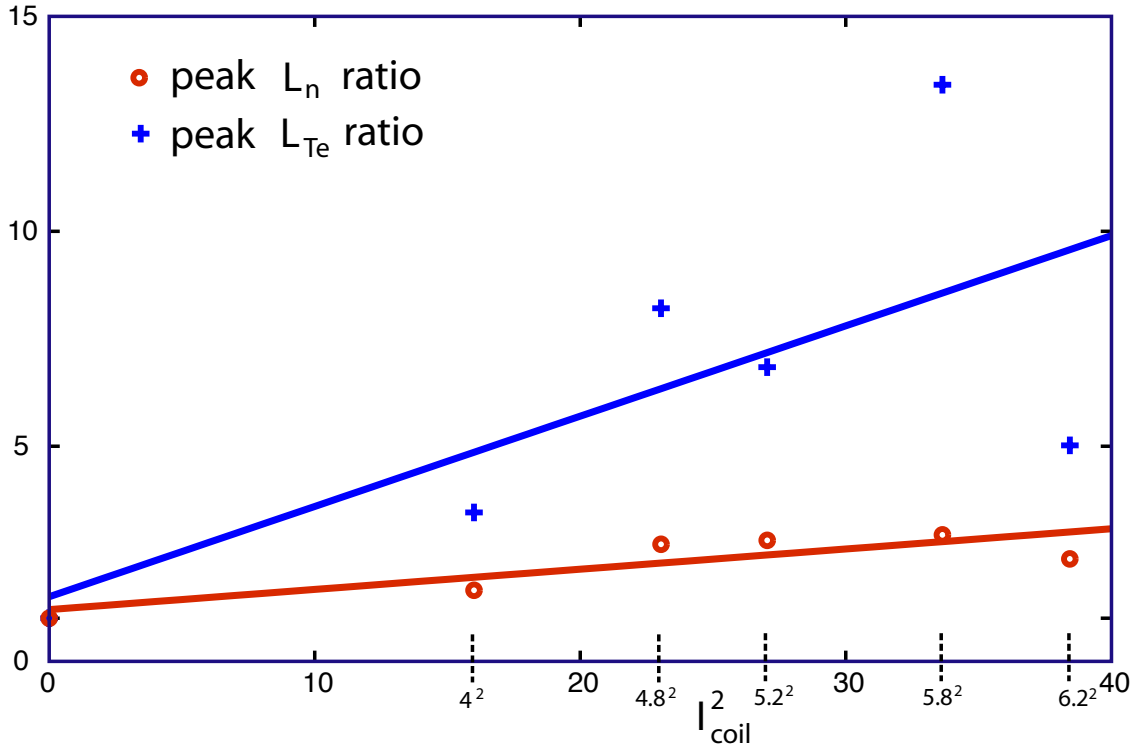

Figure 3: Peak ratios of L_{Te} and L_n with to wo RMPs vs. square of I-coil current.[2]

Toroidal Rotation Of Carbon Increases With $I_{\rm coil}$

- **When ELMs are suppressed with $I_{\rm coil} > 4.0$ kA in DIII-D ISS discharges,[4] carbon toroidal rotation at pedestal top "jumps up" to a toroidal rotation frequency of $\Omega_{\rm t} \simeq V_{\rm tor}/R \sim 10^4\,{\rm s}^{-1}$.**

- **Increases in $V_{\rm tor}$ induced by RMPs**

  do not systematically increase with $I_{\rm coil}$,

  but are always large when ELMs are suppressed ($I_{\rm coil} \geq 4.7$).

- **Changes are largest at the pedestal top:**

  near $\Psi_N \sim 0.96$.

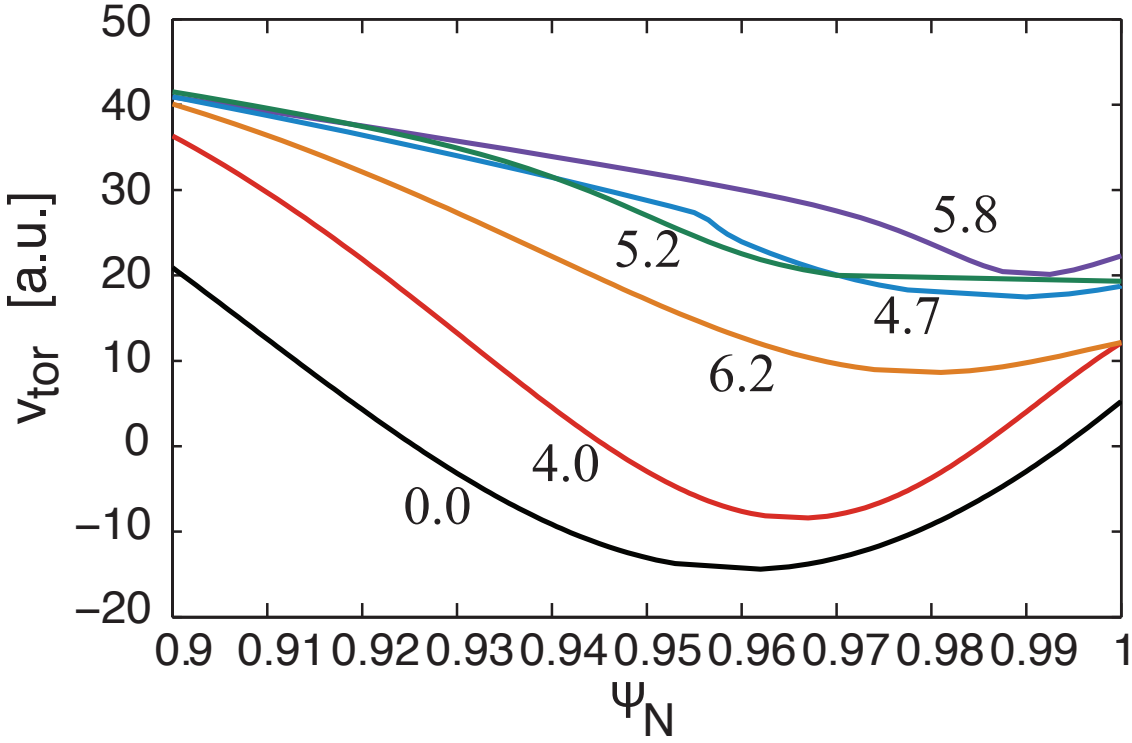

Figure 4: **Carbon toroidal rotation in edge as function of $I_{\rm coil}$. Fig. 4.19b in S. Mordijck thesis, UCSD 2011.**

Expt. Summary:[2] There Are Some Key RMP-induced Plasma Transport Effects That Need To Be Explained

- **RMPs increase gradient scale lengths and electron diffusivities:**

  $L_{Te}, L_n \sim I_{\rm coil}^2$ **implies** $\chi_e^{\rm RMP}, D^{\rm RMP} \sim I_{\rm coil}^2$ **(**$\chi_e^{\rm RMP} \sim 4$ **m**^{2}**/s at** $I_{\rm coil} = 5.2$ **kA),**

  $L_{Te}/L_n \sim 1/3$ **implies** $D^{\rm RMP} \sim \chi_e^{\rm RMP}/3$**,**

  both are larger than values without RMPs ($\chi_e^{\rm sym} \sim 0.6$ **m**^{2}**/s), and**

  their increases are localized to pedestal top region ($0.93 \lesssim \Psi_N \lesssim 0.97$**).**

- **In DIII-D low collisionality ISS discharges[4] plasma toroidal rotation** $\Omega_{\rm t}$ **increases at pedestal top when there is ELM suppression.**

- **RMP effects apparently depend on collisionality:**

  low[4] (DIII-D) — ELMs are suppressed in narrow q_{95} **"resonance windows,"**

  high[5] (ASDEX-U) — ELMs mitigated at high density, no resonance effects.

Transport Effects Of RMPs: Flutter Or Stochasticity?

- **RMP-induced radial (ρ) magnetic perturbations δB_ρ:**

  mostly just non-resonantly spatially "flutter" the field lines, flux surfaces, but can induce stochasticity if islands are created and overlap (Chirikov).

- **Transport can be induced by magnetic flutter and stochasticity:**

  flutter causes[1] $\chi_e^{\delta B} \sim v_{Te}\,\lambda_e\,(\delta B_\rho/B_0)^2$ via finite collisional ($\sim$ Braginskii) parallel electron heat conduction, which along with perpendicular electron heat transport and multiple RMP fields produces the needed irreversibility, stochasticity causes (RR[3]) $\chi_e^{\delta B_{\rm st}} \sim v_{Te}\,L_{\|c}(\delta B_{\rm st}/B_0)^2$ via $\|$ motion along $\vec{B}_{\rm st}$.

- **But flow screening of RMP fields inhibits reconnection, island formation & overlap, and hence stochasticity—next 2 viewgraphs.**

- **Nonetheless, $\delta B_\rho \neq 0$ off rational surfaces induces flutter xport.[1]**

Flow Screening Reduces δB_ρ At Rational Surfaces, But RMPs Induce Many $\delta B_{\rho\, m/n} \neq 0$ At Pedestal Top

- Resonant $\delta B_{\rho\, 10/3}$ "screened" ($\sim\times 30$) at 10/3 surface $\Longrightarrow$ no island.
- But, other $\delta B_{\rho\, m/n}/B_0 \sim 3.3 \times 10^{-4}$ MPs are nonzero there.

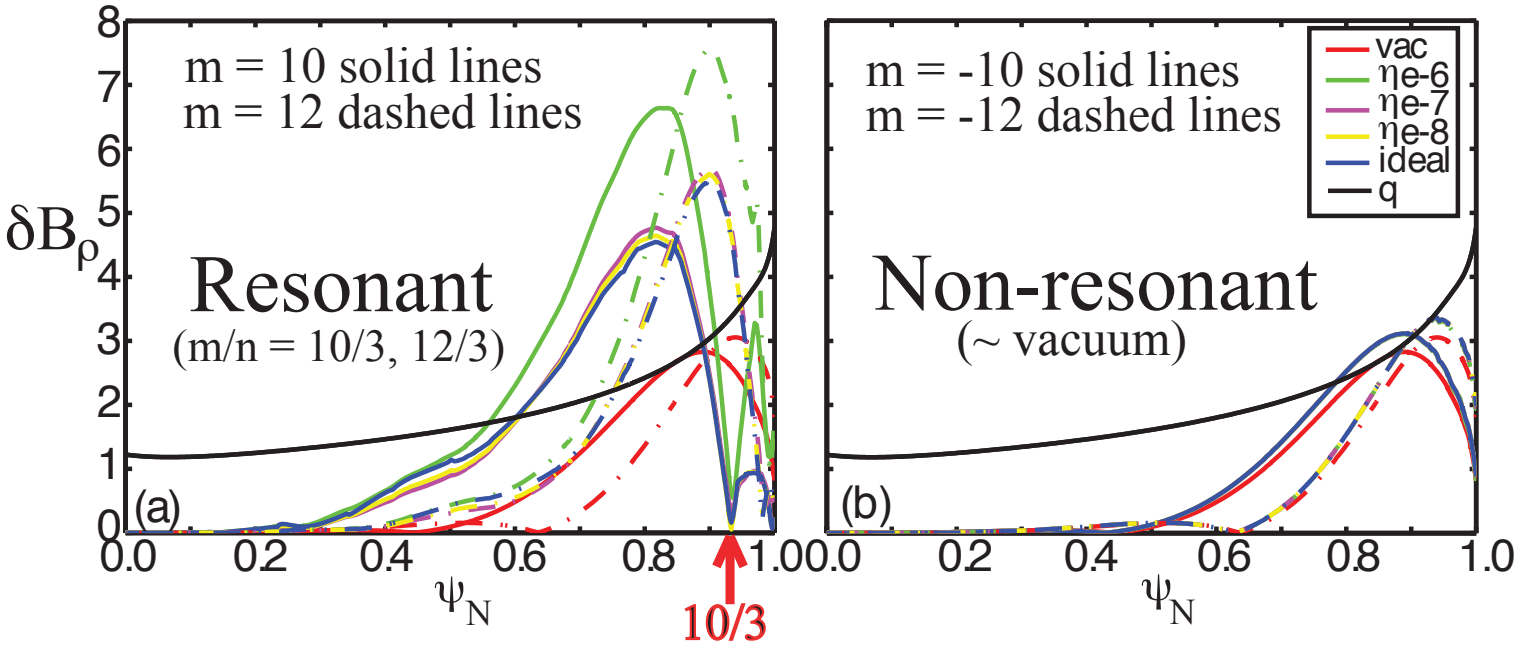

Figure 5: **Ideal/resistive MHD RMP-induced radial $\delta B_{\rho\, m/n}$ profiles: flow-screened (left), $\sim$ vacuum (right). Fig. 3 in M.S. Chu et al., Nucl. Fus. 51, 073036 (2011).**

Two-fluid Modeling[6] Yields Less Flow-Screening

- **M3D-C1 visco-resistive 2-fluid modeling[6] is more realistic. In Fig. 6 solid lines are with flow and the dashed lines are in vacuum.**

[6]N.M. Ferraro, "Calculations of two-fluid linear response to non-axisymmetric fields in tokamaks," 2011 APS-DPP invited paper JI2.02, sub. to PoP.

- **Features of say 11/3 (purple) RMP field in rotating 126440 plasma:**

  it is screened by $\sim\times 5$ near 11/3 surface,

  its amplitude grows linearly away from min,

  it extends over many m/n rational surfaces.

- **8/3, 9/3 RMP fields are not flow screened since $\vec{V}_{e\perp} \simeq 0$ at $\Psi \simeq 0.86$.**

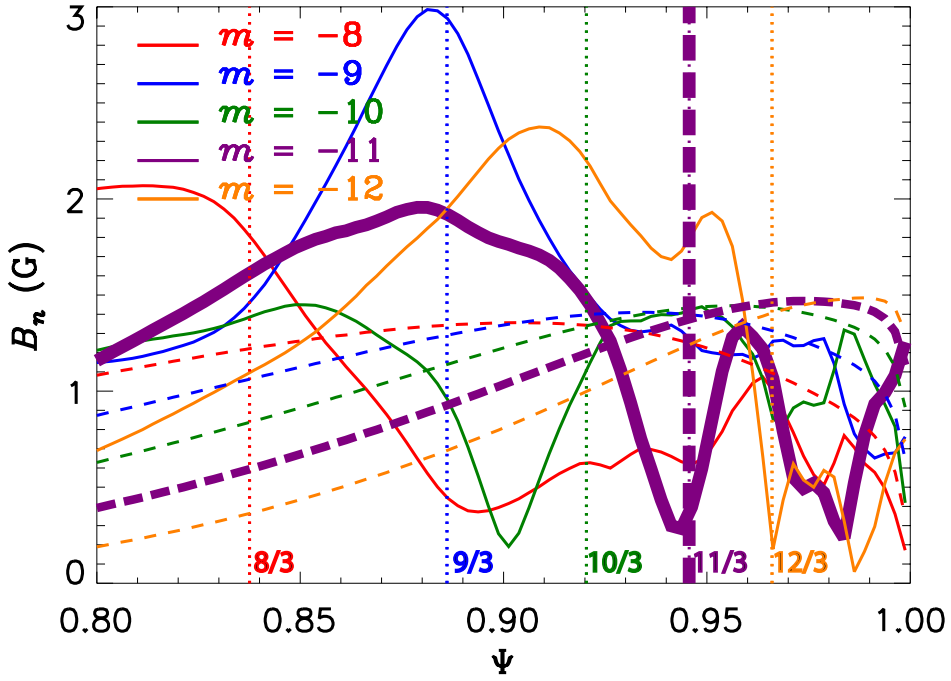

Figure 6: **Spatial variation of $\delta B_{\rho\, m/3}$ (G/kA) for 126440. Courtesy of N. Ferraro, March 2012.**

A Model Field Can Be Used For Flow-Screened δB_ρ

- **Some key characteristics of flow-screened RMP m/n fields are:**

  on rational surfaces their magnitudes are reduced from their vacuum values,

  they increase linearly with distance $|x| = |\rho - \rho_{m/n}|$ off rational surfaces,

  ideal MHD responses outside dissipative layer ($\delta_{\mu\eta} \sim 0.5$ cm) grow linearly until they reach vacuum values at cylindrical analytic estimate of $|x| \sim 1/k_\theta$.

- **Define a flow screening factor as the ratio of vacuum $\delta B_{\rho\, m/n}$ to its flow-screened value on the rational flux surface $q(\rho_{m/n}) \equiv m/n$:**

$$f_{\rm scr} \equiv \left[\frac{\delta B^{\rm vac}_{\rho\, m/n}}{\delta B^{\rm plasma}_{\rho\, m/n}}\right]_{\rho_{m/n}}$$

flow screening factor[2] in the plasma (≥ 1),

∞ (ideal MHD), ~ 30 (res. MHD), ~ 4 (2-fluid[6]).

- **Cyl. model of flow-screened m/n RMP in plasma is[2] ($|x| < 1/k_\theta$)**

$$\frac{\delta B^{\rm plasma}_{\rho\, m/n}(x)}{\delta B^{\rm vac}_{\rho\, m/n}(\rho_{m/n})} = \sqrt{1/f^2_{\rm scr} + k^2_\theta x^2} \simeq \begin{cases} 1/f_{\rm scr}, & |x| \ll 1/k_\theta f_{\rm scr}, \\ k_\theta |x|, & 1/k_\theta f_{\rm scr} \ll |x| \leq 1/k_\theta. \end{cases}$$

What Physics Causes Magnetic Flutter Transport?[1,2]

- **Consider parallel heat conduction in a perturbed $\vec{B}$ field:**

  Represent magnetic field by axisymmetric $\vec{B}_0$ plus RMP field: $\vec{B} = \vec{B}_0 + \delta\vec{B}$.

  Radial perturbation $\delta\hat{B}_{\rho\, m/n}(x)\cos(m\theta - n\zeta)$ induces $\|$ heat flow along $\vec{B}$ near m/n surface for $T_e = T_e(\rho)$ and neglecting magnetic shear $[k_\|(x) v_{Te} < \nu_e]$:

$$\delta\vec{q}_{\|m/n} \equiv -n\,\chi_\| \left(\frac{\vec{B}\vec{B}}{B^2}\cdot\vec{\nabla}T\right) \simeq -n\,\chi_\|\,\vec{B}\,\frac{\delta\hat{B}_{\rho\, m/n}}{B_0^2}\cos(m\theta - n\zeta)\,\frac{dT}{d\rho} \equiv \frac{\vec{B}_0 + \delta\vec{B}}{B_0}\,\delta q_{\|m/n}.$$

  Average radial $(\hat{\vec{e}}_\rho\cdot)$ heat flow induced by collisional $\|$ heat flow along $\vec{B}$ is

$$\langle \hat{\vec{e}}_\rho\cdot\vec{q}\rangle \equiv \langle \hat{\vec{e}}_\rho\cdot\frac{\vec{B}_0 + \delta\vec{B}}{B_0}\,\delta q_{\|m/n}\rangle = \langle\, \delta\hat{B}_{\rho\, m/n}\cos(m\theta - n\zeta)\,\delta q_{\|m/n}\,\rangle.$$

  This results in a radial electron thermal diffusivity of[1,2]

$$\boxed{\chi_e^{m/n} = \frac{1}{2}\left(\frac{\delta\hat{B}_{\rho\, m/n}}{B_0}\right)^2 \chi_{e\|},}$$

  which is to be summed over all mn magnetic perturbations.

- **Very small RMP-induced fields can induce significant $\chi_e^{m/n}$ values:**

  For DIII-D pedestal[2] $\chi_{e\|} \sim 10^{10}\,\frac{\mathrm{m}^2}{\mathrm{s}}$, so $\frac{\delta\hat{B}^{\mathrm{vac}}_{\rho\, m/n}/B_0}{f_{\mathrm{scr}}} \gtrsim 10^{-5}$ yields $\chi_e^{m/n} \gtrsim 1\,\frac{\mathrm{m}^2}{\mathrm{s}}$.

- **But magnetic shear reduces effective $\chi_{e\|}$ for $|x| > \delta_\| \sim 0.2$ cm.**

Various Spatial Scale Lengths Can Be Important

- **Radial distances from 11/3 rational surface in terms of the radial coordinate $\rho \equiv \sqrt{\psi_t/\pi B_{t0}}$ for DIII-D pedestal top parameters[2] (distances on outboard mid-plane are about half these numbers):**

ion sound gyroradius	$\rho_S \sim 0.2$ **cm**
width for small magnetic shear effects on $\chi_{e\|\|}$	$\delta_{\|\|} \sim 0.2$ **cm**
resistive MHD layer width	$\delta_\eta \sim 0.2$ **cm**
visco-resistive (2-fluid[6]) MHD layer width	$\delta_{\mu\eta} \sim 0.5$ **cm**
$\chi_{e\perp}$ **causes** T_e **to not follow island topology[7]**	$W_c^{Te}/2 \sim 0.5$ **cm**
magnetic island half-width (for $f_{\rm scr} = 4$**)**	$W/2 \sim 0.7$ **cm**
distance between rational surfaces	$1/nq' \sim 2.8$ **cm**
radial extent of $\delta B^{\rm plasma}_{\rho\, m/n}(x)$ **increasing with** $\|x\|$	$1/k_\theta \sim 6.7$ **cm**

[7] R. Fitzpatrick, "Helical temperature perturbations associated with tearing modes in tokamak plasmas," Phys. Plasmas **2**, 825 (1995).

Flutter Transport Model Employs Some Assumptions

1) RMP-induced perturbations are gyroradius small: $\delta B_\rho/B_0 \sim \rho_S/R_0 \lesssim 10^{-3}$. Effects are linearly independent, quasilinear-type.

2) Use flow-screened RMPs from linear extended MHD codes — explore self-consistency with nonlinear RMP-induced torque later.

3) If magnetic islands are present, they are thin, isolated ones that do not overlap. (Model okay outside islands that do occur.)

4) Significant perpendicular electron heat transport and multiple flow-screened RMP responses occur at each radius ρ, which causes T_e and n_e to be $\sim$ constant on axisymmetric flux surfaces.

5) Significant flow-screened RMP-flutter responses extend radially over a number of rational surfaces: $\Delta m \simeq 2nq'/k_\theta$ (~ 5).

RMP-flutter Induces Radial Electron Heat Transport[2]

- A cylindrical screw pinch model of the radial plasma transport induced by RMP-induced flutter has been developed;[2] it yields

$$\chi_e^{\rm RMP} \equiv \sum_{mn} \chi_e^{m/n}, \qquad D_e^{\rm RMP} \lesssim \chi_e^{\rm RMP}/2.5,$$

$$\boxed{\chi_e^{m/n} \equiv \chi_{m/n}^{\rm ref}\, F_{m/n}(x), \quad \text{reference } \chi_{m/n}^{\rm ref} \text{ times spatial factor } F_{m/n},}$$

$$\boxed{\chi_{m/n}^{\rm ref}} \equiv \frac{1}{2}\left[\frac{\delta \hat{B}_{\rho\, m/n}^{\rm vac}}{B_0}\right]^2 \chi_{\|{\rm c}}^{\rm ref}\left[k_\theta \delta_{\|{\rm c}}\right]^2_{\rho_{m/n}} \boxed{\simeq 0.086 {\rm m}^2/{\rm s} \text{ at DIII-D pedestal top},^2}$$

$$\chi_{\|{\rm c}}^{\rm ref} \simeq \frac{5}{4}\left[\frac{\langle n_{ut}\rangle}{n_0}\right]^3 \nu_e \lambda_e^2 \sim 1.45\times 10^9\, {\rm m}^2/{\rm s}, \sim \text{Braginskii with } ut \text{ particles},$$

$$\delta_{\|{\rm c}} \simeq \left[\frac{\langle n_{ut}\rangle}{n_0}\right]^{-2} \frac{\sqrt{2}\, L_S}{k_\theta \lambda_e} \sim 0.22\,{\rm cm}, \quad \lambda_e \equiv \frac{v_{Te}}{\nu_e}, \text{ electron collision length},$$

$$\boxed{F_{m/n}(x)} \equiv \frac{1}{[k_\theta \delta_{\|{\rm c}}]^2}\left[\frac{\delta \hat{B}_{\rho\, m/n}(x)^{\rm plasma}}{\delta \hat{B}_{\rho\, m/n}(\rho_{m/n})^{\rm vac}}\right]^2 \underbrace{\frac{\chi_{e\|}^{\rm eff}(x)}{\chi_{\|{\rm c}}^{\rm ref}}}_{1/(1+x^2/\delta_{\|{\rm c}}^2)} \simeq \frac{1/k_\theta^2 f_{\rm scr}^2 + x^2}{\delta_{\|{\rm c}}^2 + x^2},$$

in which $x \equiv \rho - \rho_{m/n}$ is radial distance off the rational surface.

Spatial Factor $F_{m/n}(x)$ Varies Significantly & Is Important

- $F_{m/n}(x)$ has different scalings in various radial regions:

$$F_{m/n}(x) \equiv \frac{1/f_{\rm scr}^2 k_\theta^2 + x^2}{\delta_{\|\rm c}^2 + x^2} \simeq \begin{cases} 1/(\delta_{\|\rm c}^2 f_{\rm fcr}^2 k_\theta^2), & |x| \ll \delta_{\|\rm c}, \\ 1/(x^2 f_{\rm fcr}^2 k_\theta^2), & \delta_{\|\rm c} \ll |x| \ll 1/f_{\rm scr} k_\theta, \\ 1, & 1/f_{\rm scr} k_\theta \ll |x| \ll 1/k_\theta. \end{cases}$$

- This causes different behavior for various screening models:

  Resistive MHD with $f_{\rm scr} \sim 30$, $\delta_{\|\rm c} \sim 1/f_{\rm scr} k_\theta$ $\Longrightarrow$ $F_{m/n} \simeq 1 =$ constant.

  Visco-res. 2-fluid[6] MHD with $f_{\rm scr} \sim 4$ $\Longrightarrow$ highly peaked, $F_{m/n}(0) \simeq 60$.

  Collisional pedestal[5] with $\delta_{\|\rm c} \sim 1/f_{\rm scr} k_\theta \sim 2$ cm $\Longrightarrow$ also $F_{m/n} \sim 1$.

- This spatial factor has a significant effect on the T_e gradient:[2]

$$\boxed{-\frac{dT_e}{d\rho}} \simeq \frac{P_e/V'\langle|\vec{\nabla}\rho|^2\rangle}{n_e \chi_e^{\rm RMP}} = \frac{P_e/V'\langle|\vec{\nabla}\rho|^2\rangle}{n_e \sum_{mn} \chi_{m/n}^{\rm ref} F_{m/n}(x)} \boxed{\sim \frac{1}{\sum_{mn} F_{m/n}(x)}.}$$

Spatial Profile Of $F_{m/n}$ Modifies Predicted T_e Profile[2]

- Obtain T_e profile by integrating $dT_e/d\rho$ inward from 11/3 surface:

$$T_e(\rho) = T_e(\rho_{11/3}) - \int_{\rho_{11/3}}^{\rho} d\rho \; \frac{P_e/(n_e \chi^{\rm ref}_{m/n} V' \langle|\vec{\nabla}\rho|^2\rangle)}{\sum_{mn} F_{m/n}(x)}, \quad \text{average } \chi_e \sim \frac{\cdots}{-\Delta T_e/\Delta\rho},$$

which yields[2] an average $\bar{\chi}_e^{\rm RMP}$ of 0.5 m^2/s for $f_{\rm scr} = 30$ or 1.2 m^2/s for $f_{\rm scr} = 4$.

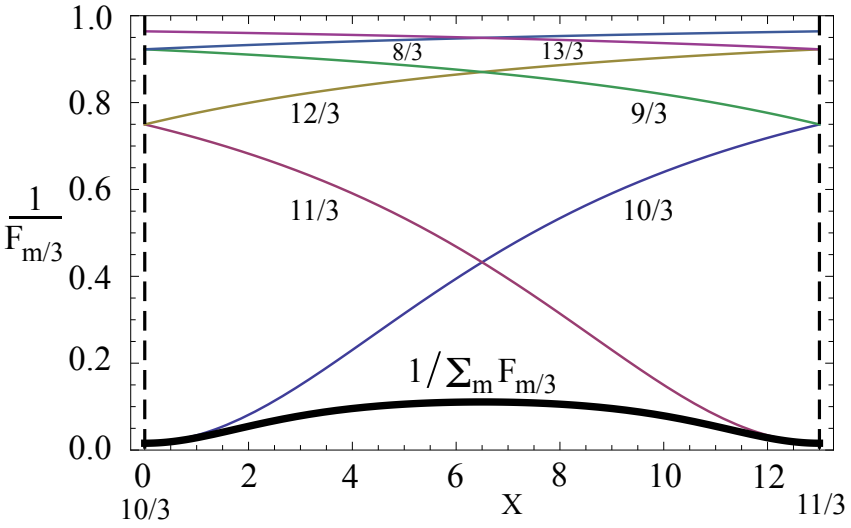

Figure 7: **Radial variation of $1/F_{m/n}$ between 10/3 and 11/3 surfaces and the inverse of their sum ($X \equiv x/\delta_{\|c}$).**

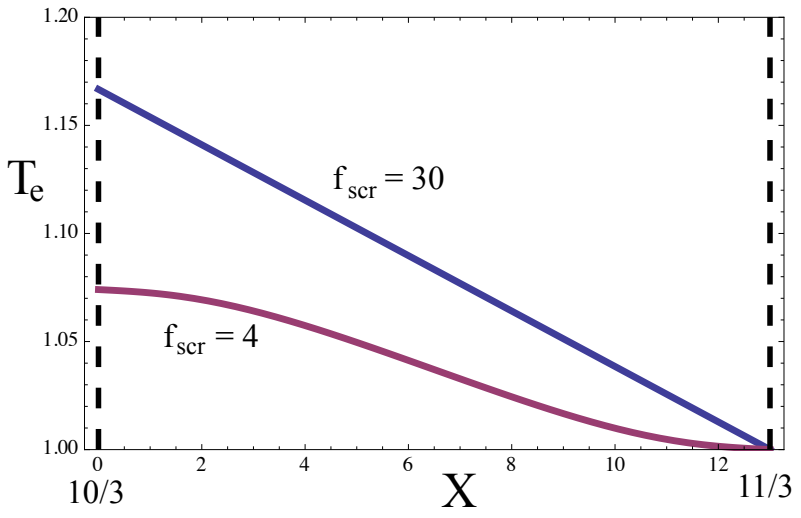

Figure 8: **T_e profiles between 10/3 & 11/3 surfaces for constant $F_{m/n}$ ($f_{\rm scr} = 30$) & due to $1/\sum_{mn} F_{m/n}(x)$ for $f_{\rm scr} = 4$.**

RMP Flutter Induces Toroidal Torques On Edge Plasma

- Plasma toroidal momentum balance[8] for $L_{\rm t} \equiv m_i n_i \langle R^2 \rangle \Omega_{\rm t}$ is:

  $$\frac{\partial L_{\rm t}}{\partial t} = \sum T_\zeta, \text{ torques } T_\zeta \equiv -\, q_s \langle \vec{\Gamma}_s \cdot \vec{\nabla} \psi_{\rm p} \rangle \text{ caused by non-ambipolar fluxes } \vec{\Gamma}_s.$$

- Ion & electron 3D density fluxes cause oppositely directed torques:

  $\vec{\Gamma}_i$ (NTV, ripple) create[8] counter-current torques because $q_i = +\,e$ ($J_\rho < 0$), whereas electron density fluxes create co-current torques because $q_e = -\,e$.

- RMP-flutter induces a non-ambipolar radial electron density flux and hence a co-current torque (for offset frequency $\Omega_{\rm fl} > \Omega_{\rm t}$):

  $$T_\zeta^{\rm RMP} \equiv e \langle \vec{\Gamma}_e^{\rm RMP} \cdot \vec{\nabla} \psi_p \rangle \simeq n_e m_i \langle R^2 \rangle \nu_e \frac{L_S^2}{6 \rho_S^2} \frac{B_{\rm p}^2}{B_0^2} \left(\sum_{mn} \frac{\delta \hat{B}^{\rm vac\ 2}_{\rho\, m/n}}{B_0^2} F_{m/n} \right) (\Omega_{\rm fl} - \Omega_{\rm t}),$$

  $$\text{flutter offset freq. } \Omega_{\rm fl} \simeq -\frac{1}{n_e e} \frac{dP}{d\psi_{\rm p}} \sim 10^4 \text{ s}^{-1} \ (> 0 \Longrightarrow \vec{V}^{\rm t}_{e\perp} \simeq -\frac{c_{T_{\rm t}}}{e B_0} \frac{dT_e}{d\rho}).$$

- Low ν_e RMP-induced torque is localized near rational surfaces.

[8] See Eqs. (3)–(7) in J.D. Callen, "Effects of 3D magnetic perturbations on toroidal plasmas," Nucl. Fusion **51**, 094026 (2011).

Cylindrical Model Has Been Compared[2] To DIII-D Results

- **Flutter predictions in qualitative agreement with experiment are:**

  scaling of $\chi_e^{\rm RMP}$ and $D^{\rm RMP}$ with $\delta B_\rho^2 \sim I_{\rm coil}^2$,

  ratio of $D^{\rm RMP}/\chi_e^{\rm RMP} \lesssim 1/3$, and

  RMP-induced change in toroidal rotation (E_ρ) to $\Omega_{\rm t} \sim 10^4$ s^{-1}.

- **But cylindrical $\chi_e^{\rm RMP}$ is smaller than experiment at pedestal top:**

  in DIII-D $\chi_{e\,\rm exp}^{\rm RMP} \sim 4$ m^2/s (#126440, 5.2 kA) while $\chi_{e\,\rm exp}^{\rm sym} \sim 0.6$ m^2/s (#126443),

  versus $\chi_e^{\rm RMP} \equiv \sum_{m,n} \chi_{m/n}^{\rm ref} F_{mn}(x) \sim (5\text{–}12)(10^{-7})\,(10^6) \lesssim 0.5\text{–}1.2$ m^2/s;

  but should use and sum flow-screened $\delta\hat{B}_{\rho\,m/n}^{\rm plasma}(x)$ + all possible mn fields.

- **Additional routes to improved agreement with experiment:**

  toroidal model could increase magnitude of $\chi_e^{\rm RMP}$ with

  $q_{95} \sim 3.5$ resonance if 10/3, 11/3, 12/3 RMP responses are modified.

Toroidal Model Yields $\|$ Flows & Radial Transport Fluxes

- **RMP-induced parallel electron flow and conductive heat flux are**[9] **($y \equiv v^2/v_{Te}^2$)**

$$\begin{bmatrix} n_e\,\delta V_{e\|} \\ \delta q_{e\|} \end{bmatrix} = \int_u d^3v\, v_\| \begin{bmatrix} L_0^{(3/2)} \\ -L_1^{(3/2)} T_e \end{bmatrix} \delta f_e = -\,2\pi \frac{B_0}{B_{\max}} \int_0^\infty v^3 dv \begin{bmatrix} 1 \\ T_e(y-\frac{5}{2}) \end{bmatrix} \int_0^1 d\lambda\, |\mathcal{R}e\{\delta h_u\}|.$$

- **These RMP-induced $\|$ flows cause radial electron density and heat fluxes:**

$$\begin{bmatrix} \delta\Gamma_{e\rho}^{m/n} \\ \delta\Upsilon_{e\rho}^{m/n} \end{bmatrix} \equiv \begin{bmatrix} \langle \delta\vec{\Gamma}_e \cdot \vec{\nabla}\rho \rangle \\ \langle \delta\vec{q}_e \cdot \vec{\nabla}\rho \rangle \end{bmatrix} = \left\langle \int_u d^3v\, \delta f_e \begin{bmatrix} 1 \\ T_e(y-\frac{5}{2}) \end{bmatrix} \vec{v}_g \cdot \vec{\nabla}\rho \right\rangle = \left\langle \int_u d^3v\, \delta h_u\, v_\| \begin{bmatrix} 1 \\ T_e(y-\frac{5}{2}) \end{bmatrix} \frac{\delta\vec{B}\cdot\vec{\nabla}\rho}{B_0} \right\rangle$$

$$= \left\langle \begin{bmatrix} n_e\,\overline{\delta V_{e\|}} \\ \overline{\delta q_{e\|}} \end{bmatrix} \frac{\delta\vec{B}\cdot\vec{\nabla}\rho}{B_{t0}} \right\rangle = -\,n_e \begin{bmatrix} D_e^{m/n} & D_T^{m/n} \\ \chi_n^{m/n} & \chi_e^{m/n} \end{bmatrix} \cdot \begin{bmatrix} d\ln p_e/d\rho - (e/T_e) d\Phi_0/d\rho \\ dT_e/d\rho \end{bmatrix}.$$

- **Transport coefficients here are defined by kinetic coefficients matrix K_{ij}:**

$$\boxed{\begin{bmatrix} D_e^{m/n} & D_T^{m/n} \\ \chi_n^{m/n} & \chi_e^{m/n} \end{bmatrix} = \frac{v_{Te}^2}{\nu_e} \frac{1}{2} \left(\frac{\langle \delta B_{\rho\, n} \rangle}{B_{t0}} \right)^2 \begin{bmatrix} K_{00} & K_{01} \\ K_{10} & K_{11} \end{bmatrix},}$$

$$\begin{bmatrix} K_{00} & K_{01} \\ K_{10} & K_{11} \end{bmatrix} = \frac{B_{t0}}{B_{\max}} \int_0^\infty \frac{dy\, y^3 e^{-y}}{2\sqrt{\pi}} \int_0^1 d\lambda\, |\mathcal{R}e\{\Lambda\}| \begin{bmatrix} 1 & y-\frac{5}{2} \\ y-\frac{5}{2} & (y-\frac{5}{2})^2 \end{bmatrix}, \quad \text{in which } y \equiv v^2/v_{Te}^2.$$

[9] J.D. Callen, A.J. Cole and C.C. Hegna, "Magnetic-perturbation-induced plasma transport in H-mode pedestals," UW-CPTC 11-15, to be at `http://www.cptc.wisc.edu` "soon."

Kinetic Matrix Coefficients K_{ij} Result From Λ Solutions

- Resultant kinetic coefficients and their regimes of applicability are

$$|k_\parallel| \simeq 0: \qquad \left[\begin{array}{cc} K_{00} & K_{01} \\ K_{10} & K_{11} \end{array}\right]^{k_\parallel=0} = \frac{2}{3\sqrt{\pi}} f_c \frac{B_{\max}}{B_{\rm t0}} \left[\begin{array}{cc} 6 & 9 \\ 9 & 75/2 \end{array}\right], \quad \text{for } y < \frac{1}{|X_{\rm t}|^{1/2}} \text{ in which } X_{\rm t} \equiv \frac{x}{\delta_{\parallel {\rm t}}},$$

$$k_\parallel \neq 0: \qquad \left[\begin{array}{cc} K_{00} & K_{01} \\ K_{10} & K_{11} \end{array}\right]^{k_\parallel\neq 0} = \frac{1}{|X_{\rm t}|^{3/2}} \frac{B_{\rm t0}/B_{\max}}{8\sqrt{\pi}\,\langle v_\parallel|_{\lambda=1}/v\rangle} \left[\begin{array}{cc} 1 & -3/2 \\ -3/2 & 13/4 \end{array}\right],$$

$$\text{for } y > y_{\min} \equiv \max\left\{\frac{1}{|X_{\rm t}|^{1/2}}, \frac{1}{X_{\rm crit}^{1/2}}\right\}, \quad X_{\rm crit} \equiv \frac{B_{\rm t0}}{2B_{\max}} \frac{\lambda_e}{\bar{R}q} \simeq 22 \text{ (so } \nu_{\rm eff}^{k_\lambda} < \omega_{ut}).$$

- Normalizing the kinetic coefficients to $(13/4)K_{11}^{k_\lambda}$ and using energy smoothing[10] to develop a Padé approximation yields for the kinetic coefficient matrix

$$\boxed{\left[\begin{array}{cc} K_{00}^{\rm t} & K_{01}^{\rm t} \\ K_{10}^{\rm t} & K_{11}^{\rm t} \end{array}\right] = \frac{13}{32\sqrt{\pi}} \frac{B_{\rm t0}/B_{\max}}{\langle v_\parallel|_{\lambda=1}/v\rangle} \left[\begin{array}{cc} G_{00} & G_{01} \\ G_{10} & G_{11} \end{array}\right],}$$ in which coefficient ~ 0.38 and matrix is

$$\left[\begin{array}{cc} G_{00} & G_{01} \\ G_{10} & G_{11} \end{array}\right] = \frac{4}{13\,|X_{\rm t}|^{3/2}} \left(\frac{|X_{\rm t}|^{3/2}}{c_{\parallel {\rm t}}} \int_0^{1/|X_{\rm t}|^{1/2}} dy\, y^3 e^{-y} + \int_{y_{\min}}^{\infty} dy\, e^{-y}\right) \left[\begin{array}{cc} 1 & y-\frac{5}{2} \\ y-\frac{5}{2} & (y-\frac{5}{2})^2 \end{array}\right], \quad c_{\parallel {\rm t}} \simeq 0.94.$$

- Properties of the geometric coefficient matrix that determine diffusivities are

$$\lim_{|X|\to 0} G_{11} = \frac{150}{13\,c_{\parallel {\rm t}}} \implies \chi_{\parallel {\rm t}}^{\rm ref} \sim 3.3\times 10^{10}, \quad \text{for } |X_{\rm t}| \to \infty, \quad \frac{G_{00}}{G_{11}} \simeq \frac{4}{13} \implies \frac{D_e^{m/n}}{\chi_e^{m/n}} \simeq \frac{1}{3.25}.$$

[10] K.T. Tsang and J.D. Callen, "Smooth transition of neoclassical diffusion from the banana to Pfirsch-Schlüter regime," Phys. Fluids **19**, 667 (1976).

Toroidal Flutter Results[9] Are Similar To Cylindrical Model

- **Parallel electron thermal diffusivity on a rational surface:**

  toroidal, Lorentz collision value is larger — $\chi_{\|\mathrm{t}}^{\mathrm{ref}} \simeq 3.3{\times}10^{10}\,\mathrm{m^2/s}$, while $\chi_{\|\mathrm{c}}^{\mathrm{ref}} \simeq 1.5{\times}10^{9}\,\mathrm{m^2/s}$.

- **Layer width beyond which magnetic shear effects dominate:**

  toroidal width is smaller — $\delta_{\|\mathrm{t}} \simeq 0.11$ cm, while $\delta_{\|\mathrm{c}} \simeq 0.22$.

- **Spatial decay of effective parallel diffusivities away from rational surface:**

  toroidal decays slower with $|x| \gg \delta_{\|}$ — toroidal $G \sim |x|^{-3/2}$, while cylindrical $\chi_{e\|}^{\mathrm{eff}} \sim |x|^{-2}$.

- **Magnitude of a single $\chi_e^{m/n}$ midway between rational surfaces:**

  using $\delta B_{\rho\, m/n}^{\mathrm{plasma}}(x)$ on p 10, they are about equal — $\chi_{e\,\mathrm{t}}^{m/n} \sim 0.23\,\mathrm{m^2/s}$, while $\chi_{e\,\mathrm{c}}^{m/n} \sim 0.21\,\mathrm{m^2/s}$;
  but using $\delta B_{\rho\,11/3}^{\mathrm{plasma}}(x)$ profile from Fig. 6, both estimates give $\chi_e^{11/3} \sim 2\ \mathrm{m^2/s}$ at $\Psi_N \sim 0.955$.

- **Ratio of RMP-induced electron density to electron thermal diffusivity:**

  results are similar — $D_{e\,\mathrm{t}}^{m/n}/\chi_{e\,\mathrm{t}}^{m/n} \simeq 1/3.25$, while $D_{e\,\mathrm{c}}^{m/n}/\chi_{e\,\mathrm{c}}^{m/n} \simeq 1/2.5$.

- **Radial RMP-flutter-induced electron transport fluxes:**

  toroidal fluxes have off-diagonal K_{ij} matrix elements, while cylindrical model fluxes don't.

Some Predictions Are Different At High Collisionality

- **ASDEX-U[5] electron collision frequency ν_e is $\gtrsim \times 10$ greater which**

  1) increases shear-effects width parameter by a factor $\sim \times 10$ to $\delta_{\|} \sim 2$ cm,

  2) increases reconnection layer width by a factor ~ 2 to $\delta_{\mu\nu} \sim 1$ cm,

  3) causes most "smoothing" processes to exceed half of the distance between rational surfaces and hence overlaps the effects around various m/n surfaces — this causes q_{95} resonance effects and magnetic islands to be less likely.

- **Model predictions for approximate ASDEX-U conditions are:**

  1) $\chi_e^{\rm RMP} \simeq \dfrac{\nu_e L_S^2}{2} \displaystyle\sum_{mn} \left[\dfrac{\delta \hat{B}^{\rm vac}_{\rho\, m/n}}{B_0}\right]^2 \gtrsim 1\ {\rm m}^2/{\rm s}, \quad L_S \equiv \dfrac{R_0 q}{s}$ **magnetic shear length,**

  2) which reduces gradients throughout the pedestal if it exceeds a typical level of $D_\eta \sim \nu_e \delta_e^2$ transport there and yields an ELM mitigation criterion:

$$\delta_e^2 \equiv \frac{c^2}{\omega_{pe}^2} \simeq \frac{3\times 10^{19}}{n_e}\, 10^{-6} \lesssim \frac{L_S^2}{2} \sum_{mn} \left[\frac{\delta \hat{B}^{\rm vac}_{\rho\, m/n}}{B_0}\right]^2 \implies n_e \gtrsim 5 \times 10^{19}\ {\rm m}^{-3}?$$

Summary

- **Experimental effects of ELM-suppressing RMPs on pedestals are:[2]**

  reduced $|\vec{\nabla}P|$ at top via increasing L_{Te} ($\lesssim\times 6$) & L_n ($\lesssim\times 2$) $\propto I^2_{\rm coil}$, Ω_t change.

- **Flow screening inhibits RMPs in forming islands, stochasticity.**

- **But RMP-flutter induces[1,2] radial transport at pedestal top:**

  both cylindrical[2] screw pinch and toroidal[9] models have been developed — results are qualitatively similar and differ quantitatively mostly by $\lesssim\times 2$,

  in high collisionality pedestals q_{95} resonances and islands are less likely.

- **Comparison between flutter model predictions and DIII-D data:[2]**

  $\chi_e^{\rm RMP} \propto I^2_{\rm coil}$, $D^{\rm RMP}/\chi_e^{\rm RMP} \lesssim 1/3$, $\Omega_{\rm t}$ changes agree qualitatively, but

  need increase of cyl. $\chi_e^{\rm RMP}$ by $\gtrsim \times 3$ and $q_{95} \sim 3.5$ resonance via modified 10/3, 11/3, 12/3 RMP responses ($\sim$ Fig. 6 $\delta B^{\rm plasma}_{\rho\, m/n}$ profiles might do both).

What Are Next Steps For Model Testing, Validation?

1) Use M3D-C1 flow-screened $\delta B_{\rho\, m/n}(\rho)$ to predict RMP-flutter-induced transport and compare to ONETWO interpretive transport modeling of electron thermal and density diffusivities,

to see if model magnitude, scaling are correct & it can capture q_{95} resonances.

2) Explore low versus high collisionality RMP cases with M3D-C1 RMP modeling plus ONETWO interpretive transport modeling,

to understand differences between RMP effects at low, high collisionality.

3) Employ quasilinear flutter model toroidal torque in M3D-C1 to explore its effects on toroidal rotation at the pedestal top,

to determine if flutter-induced torque plays a significant role in RMP effects.

4) Ultimately, treat toroidal rotation (radial electric field) on par with n, T transport by coupling M3D-C1 to predictive ONETWO,

to develop a predictive capability for RMP effects in ITER plasmas.

Toroidal:[9] RMP-Induced Flutter Modifies e Distribution

- Electron drift kinetic equation for $\vec{v}_g \equiv v_\parallel \vec{B}/B + \vec{v}_d$ with $\vec{B} \to \vec{B}_0 + \delta\vec{B}$ is[2,9]

$$\frac{\partial f_e}{\partial t} + \left[\frac{v_\parallel}{B}\,(\vec{B}_0 + \delta\vec{B}) + \vec{v}_d\right]\cdot\vec{\nabla} f_e + \frac{d\varepsilon}{dt}\frac{\partial f_e}{\partial \varepsilon} = \mathcal{C}\{f_e\}, \quad \varepsilon \equiv \frac{m_e v^2}{2} - e\Phi = \frac{m_e v_\parallel^2}{2} + \mu B - e\Phi.$$

- Lowest order solution is a Maxwellian constant along $\vec{B}_0$: $f_e = f_{\mathrm{M}e}(\rho, \varepsilon)$.

- For $\delta B_\rho(\vec{x}, t) \equiv \sum_n \delta B_{\rho\, n}(\rho, \theta)\, \mathcal{R}e\{e^{-i(n\alpha - \omega t + \varphi_n)}\}$, in helical coordinates ρ, θ, $\alpha \equiv \zeta - (m/n)\theta$, equation for $\delta h \equiv \delta f_e - (e/T_e)\,\delta\Phi\, f_{\mathrm{M}e}$ induced by $\delta B_{\rho\, n}$ is[9]

$$\frac{v_\parallel}{B_0}\,(\vec{B}_0\cdot\vec{\nabla}\theta)\left[\frac{\partial\, \delta h_n}{\partial\theta} + \underbrace{i\,(m - nq)}_{(d\alpha/d\theta)\,(\partial/\partial\zeta)}\,\delta h_n\right] - i(\omega - \omega_d)\,\delta h_n - \mathcal{C}\{\delta h_n\} = -\frac{v_\parallel}{B_0}\,\delta\vec{B}_n\cdot\vec{\nabla} f_{\mathrm{M}e}.$$

- Trapped particle solution solution vanishes — bounce average yields no drive because trapped particles don't carry any parallel flow over $\lambda_e \gg 2\pi R_0 q$.

- Magnitudes of frequencies indicate ω and ω_d can be neglected ($\ll \nu_{\mathrm{eff}}$):

$$v_{Te}/R_0 q \sim 3\times 10^6, \quad k_\parallel v_{Te} \sim (0\text{–}8)\times 10^6, \quad \omega \sim 10^4, \quad \omega_d \sim 10^4, \quad \nu_{\mathrm{eff}} \sim 2\times 10^5.$$

Bounce-averaging Yields[9] Non-adiabatic Response Eq.

- Neglecting ω, ω_d & operating on δh_n equation with $\int_{-\pi}^{\pi} d\theta B_0/[v_\parallel \vec{B}_0\cdot\vec{\nabla}\theta]$ yields

$$\boxed{ik_\parallel v\,\delta\bar{h}_u - 2\nu_\perp \frac{B_{\max}}{B_{t0}}\frac{\partial}{\partial\lambda}\left(\lambda\frac{\langle v_\parallel\rangle}{v}\frac{\partial\,\delta\bar{h}_u}{\partial\lambda}\right) = -\,v\,\frac{\langle\delta B_{\rho\,n}\rangle}{B_{t0}}\frac{\partial f_{Me}}{\partial\rho},}$$ in which $\langle\cdots\rangle$ is FSA,

$$k_\parallel(x) \equiv -\,\frac{n[q(\rho)-m/n]}{\bar{R}q} \simeq k'_\parallel x, \quad \lambda \equiv \frac{\mu B_{\max}}{\varepsilon}, \quad \delta\bar{h}_u = \int_{-\pi}^{\pi}\frac{d\theta}{2\pi}\delta h_u, \quad \langle\delta B_{\rho\,n}\rangle \equiv \langle\delta\vec{B}\cdot\vec{\nabla}\rho\, e^{in\alpha}\rangle.$$

- Since $\delta\bar{h}_u$ is a mostly separable function, it is useful to write it as:

$$\delta\bar{h}_u \equiv -\,D(\rho)\,V(v,\rho)\,\Lambda(\lambda,x,v), \quad \text{in which} \quad D \equiv \frac{\langle\delta B_{\rho\,n}\rangle}{B_{t0}}, \quad V = \frac{v}{\nu_\perp(v)}\frac{d\,f_{Me}}{d\rho} = \frac{v^4}{v_{Te}^4}\frac{v_{Te}}{\nu_e}\frac{d\,f_{Me}}{d\rho}.$$

- Then, equation above reduces to an equation for the pitch-angle function Λ:

$$\boxed{\frac{\partial}{\partial\lambda}\left(\lambda\frac{\langle v_\parallel\rangle}{v}\frac{\partial\Lambda}{\partial\lambda}\right) - i\left(\frac{k_\parallel v}{2\,\nu_\perp(v)}\frac{B_{t0}}{B_{\max}}\right)\Lambda = -\,1,}$$ with B.C.: 1) $\Lambda(\lambda{=}1) = 0$, 2) $\Lambda(0)$ finite.

- This equation will be solved for $\Lambda(\lambda)$ in two limits:

  $k_\parallel = 0$ — on $q = m/n$ rational surface, which will yield Braginskii-like result for $\chi_{e\parallel}$, and

  $k_\parallel \neq 0$ — for $|x| \equiv |\rho - \rho_{m/n}| \gg \delta_\parallel$ where magnetic shear effects become dominant.

Pitch-angle Function Λ Can Be Solved For[9] In Limits

- On a rational surface $k_\parallel = 0$ and Λ equation can be integrated directly:

$$\Lambda^{k_\parallel=0}(\lambda) \equiv \int_\lambda^1 \frac{d\lambda'}{\langle v_\parallel(\lambda',\theta)\rangle/v} \quad \Longrightarrow \quad \int_0^1 d\lambda\, \Lambda^{k_\parallel=0} = \int_0^1 \frac{\lambda\, d\lambda}{\left\langle \sqrt{1-\lambda\, B/B_{\max}} \right\rangle} \equiv \frac{4}{3}\frac{B_{\max}^2}{\langle B_0^2\rangle}\, f_c.$$

- For large $k_\parallel$ the solution will be localized in λ near the untrapped-trapped particle boundary where $\lambda \lesssim 1$. Thus, defining $\tilde{\lambda} \equiv 1-\lambda$, equation becomes

$$\frac{\partial^2 \Lambda^{k_\parallel\neq 0}}{\partial \tilde{\lambda}^2} - i\, 2\, k_\lambda^2 \frac{k_\parallel}{|k_\parallel|}\Lambda^{k_\parallel\neq 0} = -\frac{1}{\langle v_\parallel|_{\lambda=1}/v\rangle}, \quad \text{in which} \quad k_\lambda(x,v) \equiv \left[\frac{|k_\parallel(x)|\, v\, (B_{t0}/B_{\max})}{4\,\nu_\perp |\langle v_\parallel|_{\lambda=1}/v\rangle|}\right]^{1/2}.$$

- Complementary solutions of this equation are of form $e^{\pm\sqrt{\pm 2i}\, k_\lambda \tilde{\lambda}} = e^{\pm(1\pm i)\, k_\lambda \tilde{\lambda}}$. Boundary-layer-type particular solution that satisfies boundary conditions is

$$\Lambda^{k_\parallel\neq 0} = -\frac{(i/2k_\lambda^2)(k_\parallel/|k_\parallel|)}{\langle v_\parallel|_{\lambda=1}/v\rangle}\left[1 - e^{-k_\lambda\tilde{\lambda}}(\cos k_\lambda\tilde{\lambda} - i\frac{k_\parallel}{|k_\parallel|}\sin k_\lambda\tilde{\lambda})\right].$$

- Key parameters of this solution can be written as

$$k_\lambda(x,v) = |X_t|^{1/2}\frac{v^2}{v_{Te}^2}, \quad X_t \equiv \frac{x}{\delta_{\parallel t}}, \quad \delta_{\parallel t} \equiv \frac{c_t}{|k_\parallel'|\,\lambda_e} = \frac{c_t L_S}{k_\theta \lambda_e} \simeq 0.11 \text{ cm}, \; c_t \equiv 4\,|\langle v_\parallel|_{\lambda=1}/v\rangle|\,\frac{B_{\max}}{B_{t0}}.$$

- Pitch-angle integral of this solution for $k_\lambda\tilde{\lambda} \gg 1$ $(v^2/v_{Te}^2 \gg 1/|X_t|^{1/2})$ is

$$\int_0^1 d\lambda\, \mathcal{R}e\{\Lambda^{k_\parallel\neq 0}\} = \frac{1}{2k_\lambda^2|\langle v_\parallel|_{\lambda=1}/v\rangle|}\int_0^1 d\lambda\, e^{-k_\lambda\tilde{\lambda}}\sin k_\lambda\tilde{\lambda} \simeq \frac{1}{4\,k_\lambda^3\,|\langle v_\parallel|_{\lambda=1}/v\rangle|}.$$